A New Cell-Centered Implicit Numerical Scheme for Ions in the 2-D Axisymmetric Code Hall2De

Alejandro Lopez Ortega* and Ioannis G. Mikellides†
Jet Propulsion Laboratory, California Institute of Technology, Pasadena, CA, 91109

Abstract: We present a new algorithm in the Hall2De code to simulate the ion hydrodynamics in the acceleration channel and near plume regions of Hall-effect thrusters. This implementation constitutes an upgrade of the capabilities built in the Hall2De code. The equations of mass conservation and momentum for unmagnetized ions are solved using a conservative, finite-volume, cell-centered scheme on a magnetic-field-aligned grid. Major computational savings are achieved by making use of an implicit predictor/multi-corrector algorithm for time evolution. Inaccuracies in the prediction of the motion of low-energy ions in the near plume in hydrodynamics approaches are addressed by implementing a multi-fluid algorithm that tracks ions of different energies separately. A wide range of comparisons with measurements are performed to validate the new ion algorithms. Several numerical experiments with the location and value of the anomalous collision frequency are also presented. Differences in the plasma properties in the near-plume between the single fluid and multi-fluid approaches are discussed. We complete our validation by comparing predicted erosion rates at the channel walls of the thruster with measurements. Erosion rates predicted by the plasma properties obtained from simulations replicate accurately measured rates of erosion within the uncertainty range of the sputtering models employed.

Numerical simulations of Hall-effect thrusters (HET) are of paramount importance for supporting experimental studies, guiding design, and investigating the physical principles behind the operation of these devices. They are also required in order to replicate in-space conditions that cannot be achieved in the vacuum chambers employed in experiments and tests. While the first simplified theoretical models for capturing the behavior of plasmas in the stationary plasma thrusters (SPT) developed in the Soviet Union date from the 1970s [1-3], advanced numerical techniques were not available until the mid to late 1990s. These first techniques applied to simulate the Hall thruster discharge made use of particle-in-cell (PIC) [4] algorithms for the simulation of ion and electron motion [5]. In the PIC approach, a set of hyper-particles move in the computational domain according to Lorentz's force. Averaged quantities, such as densities and currents, are computed by accounting for the properties of the hyper-particles present in each fixed cell of the domain at each time-step. PIC approaches are usually time-consuming since a large number of hyper-particles are required to avoid excessive numerical noise. The hybrid approach attempts to reduce numerical noise and computational costs by modeling electrons using hydrodynamics formulations with heavy particles still using PIC. Equations of motion for electrons commonly neglect inertia terms, which results in the momentum equation becoming the vector form of Ohm's law. The most widely adopted of the hybrid algorithms is HPHall [6] (posteriorly upgraded to HPHall(2) [7]) as it was the first two-dimensional code to reproduce breathing mode oscillations in Hall thrusters. Simplified 0-D and 1-D models for explaining the presence of breathing mode oscillations were developed at around the same time by Fife et al. [8] and Boeuf and Garrigues [9], respectively (with Parra et al. [10] generalizing the work in [8] to 1-D later). In HPHall, an axisymmetric computational domain is employed in the PIC simulation of ion motion. The high values of the Hall parameter Ω_e allow for decoupling the motion of electrons in the directions parallel and perpendicular to magnetic field lines. Since resistivity across magnetic field lines (B-lines) is much higher (by an order of Ω_e^2) than along them, HPHall solves Ohm's law in the direction perpendicular to the magnetic field while electron temperature is considered isothermal and Boltzmann's law applied along B-lines.

In Hall2De, electron motion is modeled according to the vector form of Ohm's law and ion motion is modeled using fluid equations. Using hydrodynamics formulations for ion motion is not unique of Hall2De and was also applied in [11]. The major advantage of this methodology is the elimination of numerical noise, which happens at the expense of losing track of the individual motion of particles that can be captured in PIC approaches. The latter is relevant in the construction of far-plume models as hydrodynamics formulations may lose track of ions moving in

* Member of the Technical Staff, Electric Propulsion Group, 4800 Oak Grove Drive, Pasadena, CA, 91109, Mail Stop 125-109, Member AIAA.
† Principal Engineer, Electric Propulsion Group, 4800 Oak Grove Drive, Pasadena, CA, 91109, Mail Stop 125-109, Associate Fellow AIAA.

opposite direction to the main beam. Hall2De [12] solves the equations of motion for electrons without making any assumption on the electron temperature and potential along B-lines. In order to reduce numerical diffusion due to anisotropy of the transport coefficients along and across magnetic field lines, the computational domain is discretized in a magnetic-field-aligned-mesh (MFAM) [13,14]. Results obtained with Hall2De revealed that the quasi-1D assumptions made in HPHall are largely correct inside the channel. However, by including the cathode self consistently, Hall2De also showed that these assumptions fail near the cathode [15]. The upgrades of Hall2De reported in this manuscript are largely concerned with the ion motion and do not modify the algorithms that yield electron temperature and plasma potential.

Classical collision theory predicts resistivity values across magnetic field lines that are much larger than those required for capturing the plasma measurements reported in experiments. Since the cause of the enhanced collisionality remains unknown, numerical and analytical studies have historically accounted for this phenomenon by including an anomalous collision frequency term in the computation of transport coefficients that effectively reduces the Hall parameter. In the original HPHall simulations [6], the anomalous term was taken proportional to the magnitude of the magnetic field using Bohm's scaling [16]. The implementation followed in Hall2De consists of the cyclotron frequency multiplied by a profile that changes along the centerline of the acceleration channel and is extended two-dimensionally along magnetic field lines [15]. This profile has been modified as new experimental measurements have become available. The aim of this approach is to accurately capture the plasma properties reported in experiments and then try to gain physical insight on the mechanism driving the reduced resistivity by identifying the amount of anomalous collision frequency required in the Hall thruster and its near plume. As it is shown in our companion paper [17], we have found that large changes in the anomalous collision frequency in some regions of the thruster produce only small changes in the plasma density. This can then lead to ambiguous conclusions about the significance of the physics that drive the anomalous collision frequency.

In this paper, we report improvements in the two-dimensional ion motion algorithm in Hall2De. Section I describes the multi-fluid approach followed to distinguish between high energy and low energy ions and the complete computational implementation. We also discuss the implicit algorithm employed for evolving the solution in time, which results in a reduction in the computational cost by a factor of approximately 4. Section II presents a wide range of comparisons with experimental measurements to validate the code advancements. The effect of the anomalous collision frequency, background pressure, and multi-fluid algorithm employed is discussed in detail. To conclude, we show comparisons with erosion rate measurements at the channel walls.

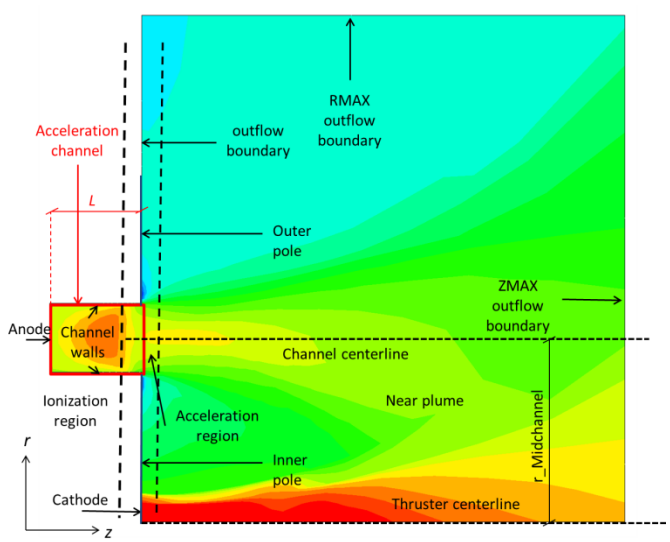

Fig. 1: Hall2De computational domain of the H6 lab thruster [18,19] showing naming conventions for the different thruster elements and plasma regions.

I. Computational method

A. Fluid equations of motion in the presence of multiple ion populations

Three regions are typically distinguished in a Hall Effect Thruster (Fig.1). Inside the channel, neutral atoms are ionized by means of collisions with electrons trapped by a magnetic field. This constitutes the ionization region. In the acceleration region, the ions are accelerated through a voltage differential to average speeds of up to 20 km/s. Depending on the geometrical configuration of the thruster and the plasma properties, there may be some overlap between these two regions, with considerable ionization taking place in the acceleration zone, which reduces the theoretical thrust that can be predicted attending to the applied voltage and the mass flow rate. The third zone is commonly called the near plume. The flow of heavy charged particles in this region consists of the main beam of accelerated ions and a secondary population of slower ions that originate at the cathode. Slow-moving ions, which originate from neutral ionization and charge-exchange processes, are also present. As the electron temperature is relatively low, the rate of ionization in the near plume decreases and becomes comparable to the charge-exchange rate. Since electric fields are weak in the near plume, these particles move much more slowly than those in the main beam.

One of the principal drawbacks of employing fluid formulations versus PIC for simulating the flow of ions in a Hall thruster is the averaging of velocities that takes place because the flow is modeled as a continuum. In the near plume, the transit time of the beam ions is lower than the time required to equilibrate the populations of low-energy ions (generated by ionization or charge exchange in the near plume region) and high-energy ions (generated in the acceleration channel). If a single-fluid formulation is used, slow ions in the near plume are convected with the mean velocity, which is dominated by the momentum of the fast ions, and results in low concentration of particles in regions that fall outside of the mean beam expansion, for instance, the poles of the thruster. Underestimation of erosion measurements at the poles may therefore occur due to the low plasma density predicted with this approach. The computed plasma potential near the poles can also be incorrect if slow ions are not accounted for properly. It is then not surprising that particle formulations, such as PIC algorithms [4] have been favored over continuum methods owing to the low collisionality of ions for the plasma conditions commonly found in Hall thrusters, even when estimates of the mean free path of ion-ion collisions computed in [12,20] postulate that a fluid approach is appropriate for modeling the ion motion in Hall effect thrusters. Particle methods are able to track the momentum of fast and slow particles independently in a way such that an average velocity is only reconstructed from averaging over the ion distribution, and is not used for convecting particles. However, these methods are prone to numerical noise whenever an insufficient number of particles is employed in the simulation, making the identification of physical oscillations challenging.

The novel approach presented here makes use of a multi-fluid algorithm to overcome the difficulties that single-fluid simulations encounter in the near plume, while eliminating statistical noise. This algorithm makes use of most of the existing features Hall2De, including a computational grid that consists of edges parallel and perpendicular to the magnetic induction field. The choice of this grid is advantageous for the computation of electron temperature and plasma potential as anisotropy of transport coefficients along and across field lines can be easily captured. As the Hall parameter for ions is small (i.e., ions are unmagnetized), this choice of grid does not offer any particular advantage for the computation of the ion motion. The algorithm below can be applied in principle to any grid. Hall2De employs a fractional-step algorithm in which equations of motion are solved consecutively in the following order: ion motion, electron temperature, plasma potential, electron current, and neutrals. In the following paragraphs, we focus on the description of the ion motion and assume that all variables not related with the ion state are known from the solution of the other equations.

In a given computational domain whose boundaries are the walls of the Hall thruster, we consider that the ion state (i.e., density and momentum) at a given time t and location $\mathbf{x}$ is obtained from the sum of the contributions of different ion species, hereinafter referred as "fluids". Ion particles pertaining to each fluid are allowed to have three different charge states (i.e., singly, doubly, and triply charged ions). Contrarily to other multi-fluid [21], multi-material [22], and multi-phase [23] approaches in which two species cannot coexist in any location (i.e., no-mixing condition), all the species can be present at any location in the computational domain of Hall2De. Determination of the fluid to which a given ion belongs is made upon examining the plasma potential at the location where the ion was generated by ionization or charge exchange. In the convention adopted in the code, fluids are numbered starting from the most energetic (in the sense that ions of this fluid are generated at a location where the potential was high

and therefore their kinetic energy increases substantially in the acceleration zone) to least energetic. "Threshold" potentials, $\phi_{th,i}$ to distinguish between fluids are not fixed and can be specified in the following manner

$$\phi_{th} = \{\phi_{th,0} = \infty, \phi_{th,1}, \ldots, \phi_{th,nF-1}, \phi_{th,nF} = -\infty\}, \tag{1}$$

with nF being the number of different fluids employed in the simulation. Thus, ionization and charge-exchange are turned on and off in the equations that model the motion of ions according to the local value of the plasma potential and how it compares to the specified threshold values. In a continuum formulation, the equations of motion that control the density and momentum of ions can be written in conservative form as follows

$$\frac{\partial n_{iC,iF}}{\partial t} + \nabla \cdot \left(n_{iC,iF}\mathbf{u}_{iC,iF}\right) = \dot{n}_{iC,iF}, \tag{2a}$$

$$\frac{\partial}{\partial t}\left(n\mathbf{u}\right)_{iC,iF} + \nabla \cdot \left(n\mathbf{u}\mathbf{u}\right)_{iC,iF} = \frac{q_{iC}n_{iC,iF}\mathbf{E}}{m_I} - \frac{kT_I}{m_I}\nabla\left(n_{iC,iF}\right) + \mathbf{R}_{elastic,iC,iF} + \mathbf{R}_{inelastic,iC,iF}, \tag{2b}$$

where n is the number density, $\mathbf{u}$ the velocity, q the charge, m_I the atomic mass of the ion species, k is Boltzmann's constant, $\dot{n}$ is the rate of gain or loss of ions through ionization and charge exchange, and $\mathbf{R}$ is the drag vector, which can be split in elastic and inelastic contributions. The indexes iC and iF denote the charge state and the fluid number in multi-fluid simulations, respectively. Ions are isothermal, with T_I being a constant value equal to the temperature of the thruster walls. Vector terms are evaluated in a z-r frame of reference as shown in Fig. 1 (left). The ionization rate reads

$$\dot{n}_{iC,iF} = b_{iF}(\phi)\left(\dot{n}_{iz,0\to iC,iF} + \sum_{jF\neq iF}\dot{n}_{CEX,iC,jF}\right) - \left(1 - b_{iF}(\phi)\right)\dot{n}_{CEX,iC,iF} + \sum_{jC<iC}\dot{n}_{iz,jC\to iC,iF} - \sum_{jC>iC}\dot{n}_{iz,iC\to jC,iF}, \tag{3}$$

The function b is dependent on the potential ϕ and takes the values

$$b_{iF}(\phi(\mathbf{x})) = \begin{cases} 1, & \text{if } \phi_{th,iF-1} \le \phi(\mathbf{x}) < \phi_{th,iF} \\ 0, & \text{otherwise} \end{cases}, \tag{4}$$

Note that ions can be lost from a fluid through charge exchange anywhere, except when $b_{iF}(\phi(\mathbf{x})) = 1$. Only binary charge exchange collisions are considered. For instance, a collision between a doubly charged ion and a neutral can only result in a complete exchange of charge. The case in which both particles become singly charged is not considered. Ionization rates are computed using the expression

$$\dot{n}_{iz,jC\to iC,iF} = n_e n_{jC,iF}\bar{c}_e\sigma_{jC,iC}, \tag{5}$$

where n_e is the electron density, $\bar{c}_e$ the mean thermal velocity of electrons, and $\sigma_{jC,iC}$ is the effective cross-section of collisions (note that $jC=0$ corresponds to collisions with neutral atoms), computed using data from Rejoub et al. [24], Bell et al. [25], and Borovik [26]. Charge exchange rates follow

$$\dot{n}_{CEX,iC,iF} = n_n n_{iC,iF} u_{iC,iF,n}\sigma_{CEX,iC,iF}, \tag{6}$$

where n_n is the neutral density, $u_{iC,iF,n}$ is the relative drift velocity between neutrals and ions of species iC,iF, and $\sigma_{CEX,iC,iF}$ is the effective collision cross section [27]. The inelastic drag term corresponds to the momentum added and subtracted due to ionization and charge exchange collisions and can be written as

$$\begin{aligned}\mathbf{R}_{inelastic,iC,iF} &= b_{iF}(\phi)\left(\dot{n}_{iz,0\to iC,iF} + \sum_{jF=1,nF}\dot{n}_{CEX,iC,jF}\right)\mathbf{u}_n - \dot{n}_{CEX,iC,iF}\mathbf{u}_{iC,iF} + \ldots \\ &+ \sum_{jC<iC}\dot{n}_{iz,jC\to iC,iF}\mathbf{u}_{jC,iF} - \sum_{jC>iC}\dot{n}_{iz,iC\to jC,iF}\mathbf{u}_{iC,iF}.\end{aligned} \tag{7}$$

Finally, the elastic drag term in the momentum equation models changes in the velocity of ions due to Coulomb collisions:

$$\begin{aligned}\mathbf{R}_{elastic,iC,iF} &= n_{iC,iF}\nu_{iC,iF;e}\left(\mathbf{u}_e - \mathbf{u}_{iC,iF}\right) - \sum_{jC\neq iC} n_{iC,iF}\nu_{iC,iF;jC,iF}\left(\mathbf{u}_{jC,iF} - \mathbf{u}_{iC,iF}\right) + \ldots \\ &+ \sum_{jF\neq iF}\sum_{jC=1,nC} n_{iC,iF}\nu_{iC,iF;jC,jF}\left(\mathbf{u}_{jC,jF} - \mathbf{u}_{iC,iF}\right).\end{aligned} \tag{8}$$

Though no major changes have been made to the remaining Hall2De conservation laws [12], we present them here for completeness. The plasma density can be computed directly once the density of all ion species is known following a quasi-neutrality assumption:

$$n_e = \sum_{iF=1,nF} \sum_{iC=1,nC} iCn_{iC,iF}. \tag{9}$$

Subsequently, the following energy equation is solved to determine the electron temperature, T_e (expressed in eV):

$$\frac{3}{2} q_e n_e \frac{\partial T_e}{\partial t} = \mathbf{E} \cdot \mathbf{j}_e + \nabla \cdot \left(\frac{5}{2} T_e \mathbf{j}_e + Q_e \right) - \frac{3}{2} T_e \nabla \cdot \mathbf{j}_e - \sum_s \Phi_s + Q_e^T, \tag{10}$$

where q_e is the absolute value of the electron charge in Coulombs, $\mathbf{j}_e$ is the electron current density, Q_e is the heat flux by particle diffusion, and Φ_s and Q_e^T account for ionization and volumetric heat exchange between electrons and heavy species due to deviations from thermal equilibrium. The electron current density is determined using Ohm's law

$$\mathbf{E} = \eta \mathbf{j}_e + \eta \Omega_e \mathbf{j}_e \times \boldsymbol{\beta} - \frac{\nabla p_e}{q_e n_e} + \eta_{ei} \bar{\mathbf{j}}_i, \tag{11}$$

with $\boldsymbol{\beta}$ an unitary vector in the direction of the magnetic field $\mathbf{B}$, $\Omega_e = |\mathbf{B}| / (n_e q \eta)$ the Hall parameter for electrons, η the resistivity, p_e the electron pressure, $\bar{\mathbf{j}}_i$ the averaged ion current density, and η_{ei} the effective ion resistivity. The resistivity is defined as

$$\eta = \frac{m_e (\nu_{ei} + \nu_{en} + \nu_{anom})}{q_e^2 n_e}, \tag{12}$$

where ν_{ei} and ν_{en} are the averaged electron-ion and electron-neutral collision frequencies. ν_{anom} is an anomalous collision frequency, added to account for the non-classical transport that has been found to persist in these devices. The current conservation equation,

$$\nabla \cdot \left(\mathbf{j}_e + \sum_{iF=1,nF} \sum_{iC=1,nC} \mathbf{j}_{iC,iF} \right) = 0, \tag{13}$$

yields the plasma potential when the electron current is substituted using Ohm's law (11).

Finally, neutral atoms do not undergo many collisions due to their long mean free path and are considered to follow straight paths from the surfaces from which they emanate (i.e., anode inflow, channel walls) towards the outflow boundaries of the computational domain. In a way similar to that used in radiation problems, view factors of each of the boundary surfaces with respect to others are computed. The neutrals proceeding from each type of boundary (i.e., anode, channel walls, thruster faces, etc.) are treated as different species and straight-line paths computed. The total neutral density and velocity is reconstructed when the contributions of the multiple "species" are added [28].

B. Computational treatment of the equations of motion for ions

A finite-volume approach is employed in the discretization of the equations of motion (2). The integral form of the equations allows us to make use of Gauss' theorem to transform the divergence terms into surface integrals

$$\int_V \left(\frac{\partial n_{iC,iF}}{\partial t} - \dot{n}_{iC,iF} \right) dV = -\int_V \nabla \cdot \left(n_{iC,iF} \mathbf{u}_{iC,iF} \right) dV = -\int_{\partial V} n_{iC,iF} \mathbf{u}_{iC,iF} \cdot \hat{\mathbf{n}} dS, \tag{14a}$$

$$\begin{aligned} &\int_V \left(\frac{\partial}{\partial t} (n\mathbf{u})_{iC,iF} - \frac{q_{iC} n_{iC,iF} \mathbf{E}}{m} - \mathbf{R}_{elastic,iC,iF} + \mathbf{R}_{inelastic,iC,iF} \right) dV = -\int_V \frac{kT_I}{m_I} \nabla \left(n_{iC,iF} \right) + \nabla \cdot \left(n\mathbf{u}\mathbf{u} \right)_{iC,iF} dV = \\ &= -\int_{\partial V} \frac{kT_i}{m_i} n_{iC,iF} \hat{\mathbf{n}} + (n\mathbf{u})_{iC,iF} \mathbf{u}_{iC,iF} \cdot \hat{\mathbf{n}} dS. \end{aligned} \tag{14b}$$

where dV and dS are infinitesimal elements of volume and area, respectively, and V is a test volume delimited by the surface ∂V with normal $\hat{\mathbf{n}}$.

1. Spatial discretization

Volume integrals are discretized in space using cell-averaged values. For each cell i in the computational domain and in semi-discrete form:

$$\int_{\square V_i} f(\mathbf{x},t)\,dV = f_i(t)\square V_i. \tag{15}$$

Most of the terms present in the volume integrals of Eq. (14) can be directly evaluated as averaged values at the cell centroids. For instance, density and momentum are evaluated in the equations as averaged cell-centered values, from which the ion velocities can be obtained. Other variables needed to compute collision frequencies and cross-sections, such as the electron temperature, are stored at the cell centers as well. The electric field and electron velocity terms demand a more careful treatment. For the electric field, we employ Gauss' theorem to obtain an averaged value in each cell

$$\mathbf{E}_i \equiv \frac{1}{\Delta V_i}\int_{\Delta V}\mathbf{E}_i dV = -\frac{1}{\Delta V_i}\int_{\Delta V}\nabla\phi dV = -\frac{1}{\Delta V_i}\int_{\partial\Delta V}\phi\hat{\mathbf{n}}dS \approx -\frac{1}{\Delta V_i}\sum_{j=1,n_{edge}}\phi_j\hat{\mathbf{n}}_j\Delta S_j\,, \tag{16}$$

where n_{edge} is the number of edges surrounding a cell (in our grid aligned with the magnetic field lines this number is always 4) and the plasma potential is evaluated at the edges. In order to obtain the plasma potential at the edges, values must be first linearly interpolated from the average potential stored at each cell. Electron currents are computed using Ohm's law (11) and stored at the edges of the computational domain in a way such that currents parallel to the magnetic field are stored in edges perpendicular to the magnetic field and viceversa. Interpolation for obtaining cell-centered currents considers this fact to obtain parallel and perpendicular currents at the cell center that are then rotated to the *z-r* frame of reference.

Surface integrals are discretized as

$$\int_{\partial V} f(\mathbf{x},t)\hat{\mathbf{n}} + \mathbf{g}(\mathbf{x},t)\cdot\hat{\mathbf{n}}dS = \sum_{j=1,n_{edge}}\left(f(t)_j\hat{\mathbf{n}}_j + \mathbf{g}(t)_j\cdot\hat{\mathbf{n}}_j\right)\Delta S_j\,, \tag{17}$$

where the index j denotes quantities evaluated at the edges. Given the hyperbolic nature of the convection terms, values at the edges cannot be linearly interpolated from cell-centered quantities, as that would render the scheme unstable. There exist multiple algorithms for estimating the inter-cell fluxes that vary in level of complexity. The method implemented here that replaces the original vertex-centered, upwind-bases approach in Hall2De [12] is a variant of the Harten-Lax-van Leer (HLL) scheme [29]. This method proposes two different expressions for evaluating the mass and momentum flux across cells attending to the sign of the characteristic speeds c (eigenvalues) of the system of equations (2):

$$\left\{c_L \equiv u - \sqrt{\frac{kT_i}{m_I}}, c_R \equiv u + \sqrt{\frac{kT_I}{m_I}}\right\}. \tag{18}$$

In our implementation, the ion speed of sound $a_I \equiv \sqrt{kT_I/m_I}$ is constant and u is the normal velocity across the edge $u = \mathbf{u}_j \times\hat{\mathbf{n}}$. If u is in absolute value greater than a_I, the flow is supersonic and the intercell fluxes, F only depend on the state of the upwind cell:

$$\begin{aligned} F_{n,HLL,j}\Delta S_j &\equiv (n\mathbf{u})_j\cdot\hat{\mathbf{n}}_j\Delta S_j = n_{upw}\mathbf{u}_j\cdot\hat{\mathbf{n}}_j\Delta S_j, \\ F_{n\mathbf{u},HLL,j}\Delta S_j &\equiv \left[(n\mathbf{u}\mathbf{u})_j\cdot\hat{\mathbf{n}}_j + \left(a_I^2 n\right)_j\hat{\mathbf{n}}_j\right]\Delta S_j = (n\mathbf{u})_{upw}\mathbf{u}_j\cdot\hat{\mathbf{n}}_j\Delta S_j + a_I^2 n_{upw}\hat{\mathbf{n}}_j\Delta S_j, \end{aligned} \tag{19}$$

where for any variable f, the *upw* subscript denotes the value of f in the upwind cell. If we label with L and R the left and right cells adjacent to an edge j in the sense that the normal vector points from the L cell to the R cell, then

$$f_{upw} = \begin{cases} f_L & \text{if } \mathbf{u}_j\times\hat{\mathbf{n}}_j > 0 \\ f_R & \text{if } \mathbf{u}_j\times\hat{\mathbf{n}}_j < 0 \end{cases}. \tag{20}$$

In the case of $|u| < a_I$, the flow is subsonic and the flux is constructed using a weighted combination of the states of the two cells adjacent to the edge, as follows:

$$F_{n,HLL,j}\Delta S_j = \left[\left(\mathbf{u}_j \cdot \hat{\mathbf{n}}_j\right)\frac{n_L + n_R}{2} + a_I \frac{n_L - n_R}{2} \right]\Delta S_j,$$
$$F_{n\mathbf{u},HLL,j}\Delta S_j = \left[\left(\mathbf{u}_j \cdot \hat{\mathbf{n}}_j\right)\frac{n\mathbf{u}_L + n\mathbf{u}_R}{2} + a_I \frac{n\mathbf{u}_L - n\mathbf{u}_R}{2} + a_I F_{n,HLL,j}\hat{\mathbf{n}}_j \right]\Delta S_j. \tag{21}$$

2. Time discretization

One major limitation of the previous ion algorithm in Hall2De was its explicit time discretization. Explicit algorithms are limited by stability constraints imposed by the Courant condition [30]. A semi-implicit predictor/multi-corrector [31] strategy is adopted here for discretizing the time evolution and reducing the limitations of the Courant condition. Because the equations are non-linear, Newton-Raphson iterations would be needed for constructing a fully implicit scheme, which is time-consuming. In the approach presented here, the non-linear terms are evaluated using the last guess of the multi-corrector, which reduces the problem to the solution of a linear system of equations at each iteration. Our numerical tests have shown that three iterations are typically enough for achieving convergence and being able to significantly relax the Courant condition. The fully discretized form of the equations of motion reads

$$\left(\frac{n_i^{t+\Delta t,(i)} - n_i^t}{\Delta t} - \dot{n}_i^{t+\Delta t,(i-1)} \right)\Delta V_i = -\sum_{j\neq b} F_{n,HLL,j}^{t+\Delta t,(i),(i-1)}\Delta S_j - \sum_{j=b} F_{n,b}^{t+\Delta t,(i),(i-1)}\Delta S_b, \tag{22a}$$

$$\left(\frac{n\mathbf{u}_i^{t+\Delta t,(i)} - n\mathbf{u}_i^t}{\Delta t} - R_{elastic,i}^{t+\Delta t,(i-1)} - R_{inelastic,i}^{t+\Delta t,(i-1)} \right)\Delta V_i = -\sum_{j\neq b} F_{n\mathbf{u},HLL,j}^{t+\Delta t,(i),(i-1)}\Delta S_j - \sum_{j=b} F_{n\mathbf{u},b}^{t+\Delta t,(i),(i-1)}\Delta S_b, \tag{22b}$$

where we have omitted the subscripts *iC,iF* for simplicity, and the subscript *b* denotes evaluation at a boundary edge. This formulation preserves mass and linear momentum in the absence of source terms as the discretization of the surface integrals represent transfers of mass and momentum from cell to cell that add up to zero. We also assume that the normal to each edge points outwards from the cell *i*. Fluxes across boundary edges are specified in the next paragraph. The parenthesis superscripts *(i)* and *(i-1)* refer to the *i*-th and *(i-1)*-th iteration, respectively, of the predictor/multi-corrector algorithm. This method requires an initial estimate for density and momentum, which are given by the values at the previous time-step *t:*

$$n_i^{t+\Delta t,(0)} = n_i^t,\ n\mathbf{u}_i^{t+\Delta t,(0)} = n\mathbf{u}_i^t. \tag{23}$$

At each iteration of the method, the ion generation and drag values at each cell are computed using the values of density and momentum from the previous pass. The intercell fluxes are also discretized in time in a way such that non-linear terms depend on the variables computed at the previous pass of the predictor/multi-corrector. If the flow is supersonic,

$$F_{n,HLL,j}^{t+\Delta t,(i),(i-1)} = n_{upw}^{t+\Delta t,(i)}\mathbf{u}_j^{t+\Delta t,(i-1)} \cdot \hat{\mathbf{n}}_j,$$
$$F_{n\mathbf{u},HLL,j}^{t+\Delta t,(i),(i-1)} = \left(n\mathbf{u}\right)_{upw}^{t+\Delta t,(i)}\mathbf{u}_j^{t+\Delta t,(i-1)} \cdot \hat{\mathbf{n}}_j + a_I^2 n_{upw}^{t+\Delta t,(i-1)}\hat{\mathbf{n}}_j. \tag{24}$$

In the subsonic case,

$$F_{n,HLL,j}^{t+\Delta t,(i),(i-1)} = \left[\left(\mathbf{u}_j^{t+\Delta t,(i-1)} \cdot \hat{\mathbf{n}}_j\right)\frac{n_L^{t+\Delta t,(i)} + n_R^{t+\Delta t,(i)}}{2} + a_I \frac{n_L^{t+\Delta t,(i)} - n_R^{t+\Delta t,(i)}}{2} \right]$$
$$F_{n\mathbf{u},HLL,j}^{t+\Delta t,(i),(i-1)} = \left[\left(\mathbf{u}_j^{t+\Delta t,(i-1)} \cdot \hat{\mathbf{n}}_j\right)\frac{n\mathbf{u}_L^{t+\Delta t,(i)} + n\mathbf{u}_R^{t+\Delta t,(i)}}{2} + a_I \frac{n\mathbf{u}_L^{t+\Delta t,(i)} - n\mathbf{u}_R^{t+\Delta t,(i)}}{2} + a_I F_{n,HLL,j}^{t+\Delta t,(i-1),(i-1)}\hat{\mathbf{n}}_j \right]. \tag{25}$$

Substitution of these expressions and the boundary fluxes discussed below in Eq. (22) yields a numerical scheme that enables the computation of $n_i^{t+\Delta t,(i)}$ and the two components of $n\mathbf{u}_i^{t+\Delta t,(i)}$ by solving three independent linear systems of equations at each pass of the predictor/multi-corrector algorithm.

3. Boundary conditions

Boundary conditions are specified in the form of edge fluxes for the density and momentum equations. We distinguish three types of boundary conditions in the computational domain: cathode, sheath, and outflow.

Cathode boundary conditions typically correspond to one or two edges in the computational domain. A flux of ions is prescribed into the computational domain as a fraction of the mass flow rate of neutrals. We assume that the flux of ions consists entirely of singly charged ions and it is assigned to the least energetic fluid. For other ion species, the fluxes at this boundary are zero.

$$
\begin{aligned}
F_{n,b,iC=1,iF=nF}^{t+\Delta t,(i),(i-1)} &= -\frac{\dot{m}_{ions}}{m_I A_{cathode}}, \\
F_{n\mathbf{u},b,iC=1,iF=nF}^{t+\Delta t,(i),(i-1)} &= \left(-\frac{\dot{m}_{ions}}{m_I A_{cathode}} \left[u_{cathode} + \frac{a_I^2}{u_{cathode}} \right] \right) \begin{pmatrix} 1 \\ 0 \end{pmatrix},
\end{aligned}
\tag{26}
$$

where $A_{cathode}$ is the total exit area of the cathode and $\dot{m}_{ions}$ is the mass flow rate of ions.

Since the sheath cannot be resolved in Hall2De, an approximate sheath physics model is employed at wall boundaries. In an ion-attracting sheath, the edge velocity from the computational domain to the boundary is computed using Bohm's criterion [31] whilst in an ion repelling-sheath the edge velocity is set to zero not allowing any ion particle to escape the computational domain.

$$
\mathbf{u}_{sheath} = \hat{\mathbf{n}}_b \begin{cases} 0.607\sqrt{\dfrac{kT_{e,i,b}^t}{m_I}}, \text{ if } \phi_{b,i}^t \geq \phi_{wall} \\ 0, \text{ otherwise} \end{cases}. \tag{27}
$$

The subindex *b,i* denotes values evaluated at the cell adjacent to the boundary edge *b*. The sheath velocity is multiplied by the density and momentum of the adjacent cell to obtain the mass and momentum lost to the walls due to the sheath. In the case of the natural outflow $\mathbf{u}_{b,i}^{t+\Delta t,(i-1)} \cdot \hat{\mathbf{n}}_b$ in the absence of a sheath being larger than the sheath velocity, the natural outflow prevails over the sheath effect:

$$
\begin{aligned}
F_{n,b}^{t+\Delta t,(i),(i-1)} &= n_{b,i}^{t+\Delta t,(i)} \max\left(\mathbf{u}_{sheath} \cdot \hat{\mathbf{n}}_b, \mathbf{u}_{b,i}^{t+\Delta t,(i-1)} \cdot \hat{\mathbf{n}}_b \right), \\
F_{n\mathbf{u},b}^{t+\Delta t,(i),(i-1)} &= n\mathbf{u}_{b,i}^{t+\Delta t,(i)} \max\left(\mathbf{u}_{sheath} \cdot \hat{\mathbf{n}}_b, \mathbf{u}_{b,i}^{t+\Delta t,(i-1)} \cdot \hat{\mathbf{n}}_b \right).
\end{aligned}
\tag{28}
$$

Finally, outflow boundary conditions are applied at the edges of the computational domain where no walls exist. The conditions of the adjacent cell are extrapolated to the edge to allow particles to exit the computational domain. If the velocity at the adjacent cell points away from the boundary, no flux is allowed into the domain.

$$
\begin{aligned}
F_{n,b}^{t+\Delta t,(i),(i-1)} &= \begin{cases} n_{b,i}^{t+\Delta t,(i)} \dfrac{(n\mathbf{u})_{b,i}^{t+\Delta t,(i-1)}}{n_{b,i}^{t+\Delta t,(i-1)}} \cdot \hat{\mathbf{n}}_b, \text{ if } \dfrac{(n\mathbf{u})_{b,i}^{t+\Delta t,(i-1)}}{n_{b,i}^{t+\Delta t,(i-1)}} \cdot \hat{\mathbf{n}}_b > 0 \\ 0, \text{ otherwise} \end{cases}, \\
F_{n\mathbf{u},b}^{t+\Delta t,(i),(i-1)} &= \begin{cases} \left(n\mathbf{u}_{b,i}^{t+\Delta t,(i)} \dfrac{(n\mathbf{u})_{b,i}^{t+\Delta t,(i-1)}}{n_{b,i}^{t+\Delta t,(i-1)}} \cdot \hat{\mathbf{n}}_b + a_I^2 n_{b,i}^{t+\Delta t,(i-1)} \hat{\mathbf{n}}_b \right), \text{ if } \dfrac{(n\mathbf{u})_{b,i}^{t+\Delta t,(i-1)}}{n_{b,i}^{t+\Delta t,(i-1)}} \cdot \hat{\mathbf{n}}_b > 0 \\ 0, \text{ otherwise} \end{cases}.
\end{aligned}
\tag{29}
$$

C. **Computational performance**

Hall2De is intended to be run in workstation-class computers with typical computational domains comprising around a thousand cells. A major disadvantage of using a grid aligned to the magnetic field is that irregularly sized cells close to the walls are almost impossible to avoid. This difficulty is more relevant in magnetically shielded thrusters whose magnetic field lines graze the channel walls. Time-steps of the order of $5\text{x}10^{-9}$ s and $5\text{x}10^{-10}$ s were common in the previous version of the ion algorithm in Hall2De for unshielded and magnetically shielded thrusters, respectively. The implicit discretization in time of the equations of motion for ions now allows for stable solutions using time-steps of $3\text{x}10^{-8}$ s and $5\text{x}10^{-9}$ s in unshielded and shielded configurations, respectively. Since the new ion algorithm employs a predictor/multi-corrector iterative algorithm, new simulations with Hall2De actually run 3 to 4 times faster than previous simulations.

II. Validation and tests

The H6 (Fig. 2) is a 6kW-class thruster developed in a joint effort of the University of Michigan, the Air Force Research Laboratory (AFRL) and the Jet Propulsion Laboratory (JPL) [18,19]. It features a centerline-mounted cathode and is designed for nominal operation at 300V, discharge current of 20A, and 20 mg/s flow rate. Under these conditions, 400mN of thrust and a specific impulse of approximately 1950s have been measured. Plasma properties and erosion rates in this thruster have been extensively measured. We make use of this data here to validate the Hall2De algorithm advancements described in Section I.

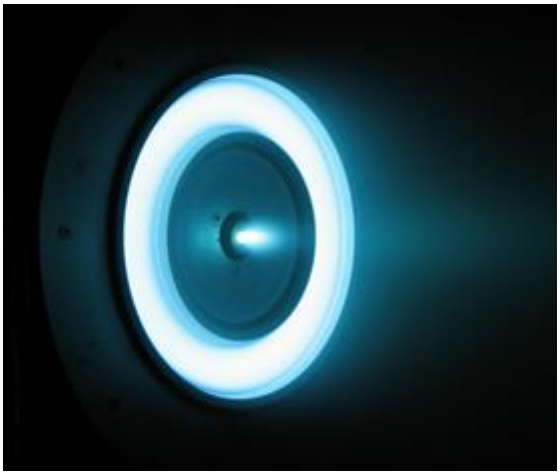

Fig. 2: H6 laboratory thruster in operation

A. Cut-off in anomalous collision frequency

Previous work by Mikellides et al. [15] showed an anomalous collision frequency map that allowed simulations to reproduce experimental measurements. This map was constructed by extension along magnetic-field lines (sometimes referred as B-lines) of a collision frequency profile defined along the centerline of the acceleration channel (Fig.3 (left)), and has evolved as new experimental results have become available. We note that the anomalous collision frequency required outside the channel is several orders of magnitude higher than that predicted by classical mechanisms and comparable to the electron cyclotron frequency, resulting in a Hall parameter close to unity. We argue here that due to the high plasma density established in the cathode plume, classical collisions of electrons with ions and neutrals occur often enough to damp out any wave motion that can lead to anomalous transport across field lines. To test this hypothesis, we set to zero the anomalous collision frequency below a magnetic field line along the cathode plume as shown in Fig. 3 (right). We find that this cut-off is necessary to reproduce the steep drop of the plasma potential near the thruster centerline (Fig. 4 (left)) that has been observed in radial measurements. The radial distributions of the plasma potential at z/L=1.19 for simulations run with a background pressure of 1.6×10^{-5} Torr. and in perfect vacuum conditions (both simulations using 2 fluids for modeling the ion flow and the same anomalous collision frequency profile) show that this feature becomes more acute in the vacuum case.

The different behavior of the plasma potential close to thruster axis between the two simulations is consistent with the value of the perpendicular resistivity across the cut-off B-lines. It can be shown from Eq. (11) that the resistivity perpendicular to the magnetic lines is proportional to the square of the Hall parameter, which indicates

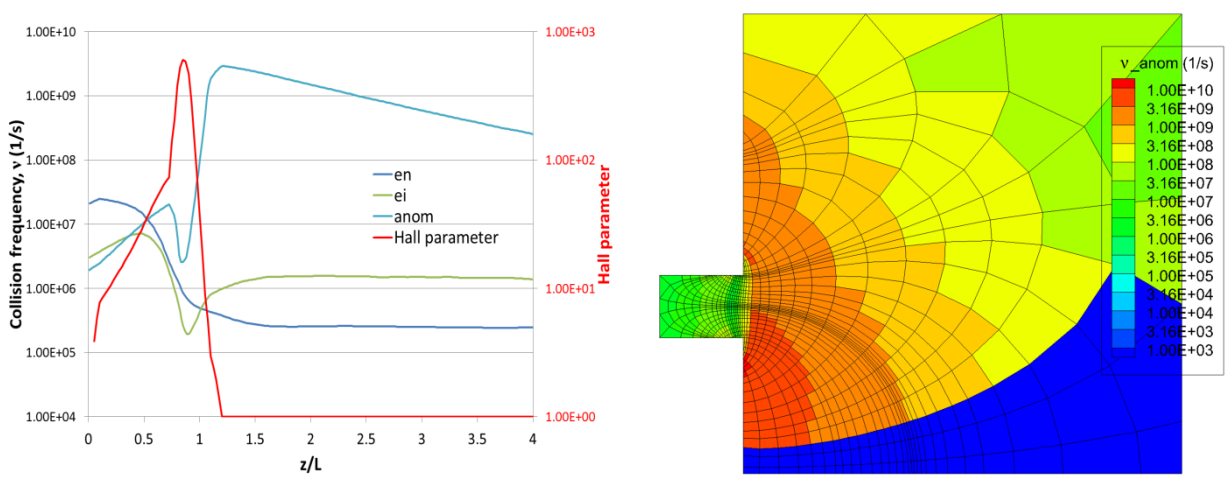

Fig. 3: Left: Typical anomalous collision frequency profile along channel centerline compared with classical collision frequencies (en: electron-neutral, ei: electron-ion), and Hall parameter. Right: 2-D contour plot of anomalous collision frequency showing cut-off region surrounding cathode (blue). Grid is aligned with magnetic field lines.

that resistance to cross magnetic field lines decreases with the square of the plasma density when assuming that electron collisions with ions dominate over collisions with neutrals. In the absence of anomalous terms and when Ω_e>>1, we can write approximately

$$\eta_\perp \approx \frac{B^2}{n_e m_e \left(\nu_{ei} + \nu_{en}\right)}, \tag{30}$$

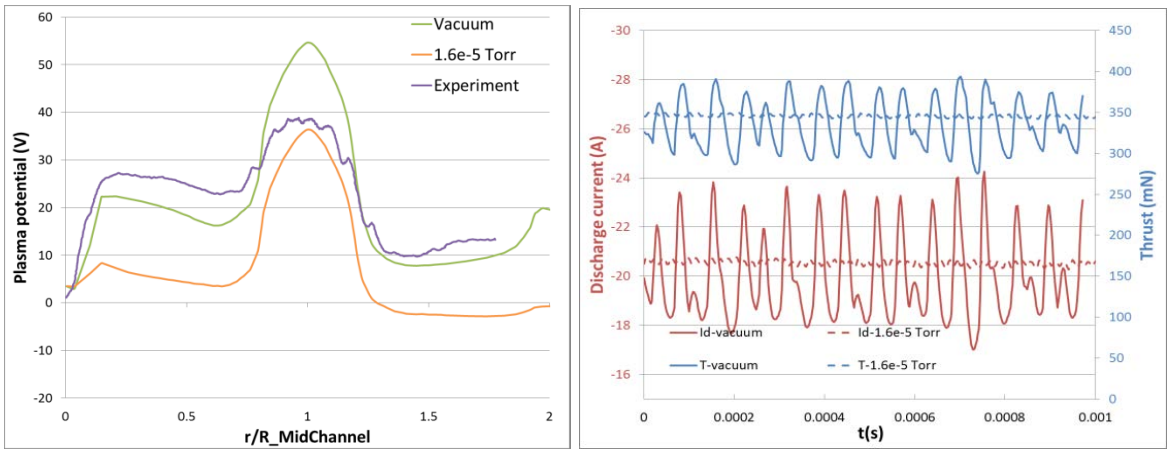

Fig. 4: Left: radial profile of plasma potential at z/L=1. Comparison between simulation results in vacuum and with background pressure of 1.6x10^{-5} Torr., and experimental measurements. Right: evolution in time of discharge current and thrust. Vacuum case exhibits oscillations of amplitude ~10% of nominal value and frequency 16kHz. Much smaller oscillations predicted in the case with background pressure.

As shown in Fig. 5, the plasma density expected in vacuum conditions decreases as a result of lower ionization rates. This leads to lower collision frequencies and higher values of the Hall parameter and resistivity perpendicular to the magnetic field. The amount of electron current that needs to cross the magnetic field lines stays relatively constant at approximately ¼ of the discharge current (the remainder being used in neutralizing the beam). Thus, the required electric field perpendicular to B-lines increases and the plasma potential exhibits the abrupt jump shown in Fig. 4(left). It is also important to note that most of the current crosses the B-line at the region of higher density (*z/L>5*), which corresponds to the location at which the main beam intersects the magnetic-field line. This was also shown in previous simulations with Hall2De [20]. Current across B-lines is also allowed close to inner pole due to the high plasma density and electron-neutral collision frequency. However, the manner the later happens in the two simulations is substantially different. As shown in Fig. 4 (right), the behavior of the discharge current, I_d and thrust, T in the case with background pressure is approximately steady in time while it is highly oscillatory in vacuum. In the first case, the values of resistivity and electric field remain approximately constant in time. The oscillations in the vacuum case appear to be closely related to cathode ions not being able to move across the potential wall. In this configuration, the resistivity close to the inner-pole is high and most current crosses the cut-off B-line at the intersection with the beam. Fig. 6 (left) depicts contour plots for plasma potential and density in this situation. Plasma density builds up at the cathode exit and, as this occurs, the pressure building at the thruster axis tries to be released by sending ions against the electric field. At some point, the ions are allowed to expand radially and the density at the cut-off B-line increases, reducing the resistivity across it. As shown in Fig.6 (right), the perpendicular electric field decreases and more current is allowed into the acceleration channel, crossing the cut-off B-line near the inner pole region. This situation corresponds to peaks in the discharge current. Subsequently, ions start to accumulate again close to the axis, restarting the cycle. The amplitude and period of the oscillations are intimately related to the jump in plasma potential as the time required to build up the plasma density required to overcome the potential wall depends on the magnitude of the electric field. The amplitude of the discharge current oscillations is proportional to the gradient of the plasma density at the cathode exit per Eq. (11). In the vacuum case, amplitude oscillations are approximately 10% of the nominal value with a frequency of 16 kHz. In vacuum chamber conditions, amplitude of oscillations is less than 1% of the nominal value at 60 kHz. The period of oscillations in the vacuum case is remarkably close to the breathing mode and further investigation is required since these results indicate that oscillations are mainly driven by the plasma potential near the cathode, which contrasts with the predator-prey mechanism between ions and neutrals postulated in [9-11].

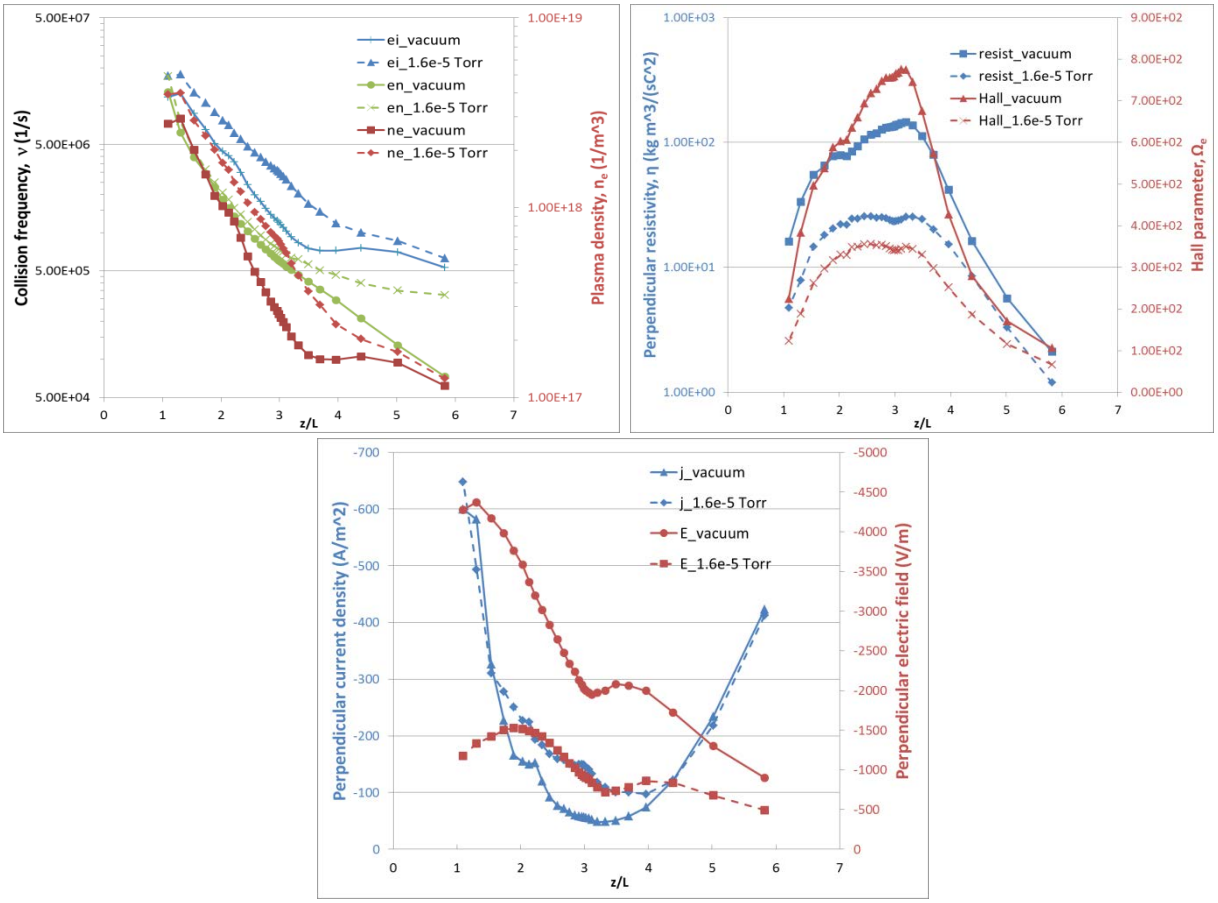

Fig. 5: Top left: Electron-ion (ei), electron-neutral (en) collision frequency and plasma density at the last B-line with zero anomalous collision frequency for simulations in vacuum and with background pressure of $1.6x10^{-5}$ Torr. Top right: Perpendicular resistivity and Hall parameter for the same simulations. The Hall parameter is considerably lower in the case with background pressure, reducing the perpendicular resistivity. Bottom: electron current density and electric field across the B-line with zero anomalous collision frequency. The current density is similar in both cases but it requires a higher electric field in the vacuum case due to increased resistivity. All results are time-averaged.

Since there exists better agreement of the experimental results (measured in finite background pressure conditions of $1.6x10^{-5}$ Torr.) with the vacuum simulation, both along the radial profile shown in Fig. 4 (left) and in the frequency of oscillations, one can argue that background pressure should not have an effect as significant as the one shown in simulation results. In the example shown above, the neutral density was considered isotropic along the boundaries of the computational domain. However, studies of the depletion of neutral gas as atoms move from the chamber walls to the thruster indicate that the neutral density at the ZMAX boundary (please refer to Fig. 1) is over-predicted as atoms reflected from the chamber walls collide with the main beam ions moving in the opposite direction. To show the effect that anisotropy of neutral density in the near plume can have, we set the neutral density at the right boundary to zero while leaving the other boundaries unchanged. With this action, there exists a lower flow of neutrals into the computational domain and ionization decreases. Fig. 7 shows that under these conditions, the radial profile for the potential approaches the experimental results and slightly larger oscillations are present in thrust and discharge current.

The main conclusion of this analysis is that the anomalous collision frequency in the cathode region (at least when the thruster has the cathode mounted at the axis) must decrease from its value in the near plume. Otherwise, the abrupt jump in plasma potential predicted by experiments cannot be captured in numerical simulations. In addition, the jump in the plasma potential is highly dependent on local plasma parameters, specifically the plasma density, as the resistivity across B-lines depends approximately on $1/n_e^2$. Small uncertainties in the way the collision frequencies are computed can have a large impact on the plasma potential in this region. Finally, oscillations in the performance variables (discharge current and thrust) are also proportional to the potential drop.

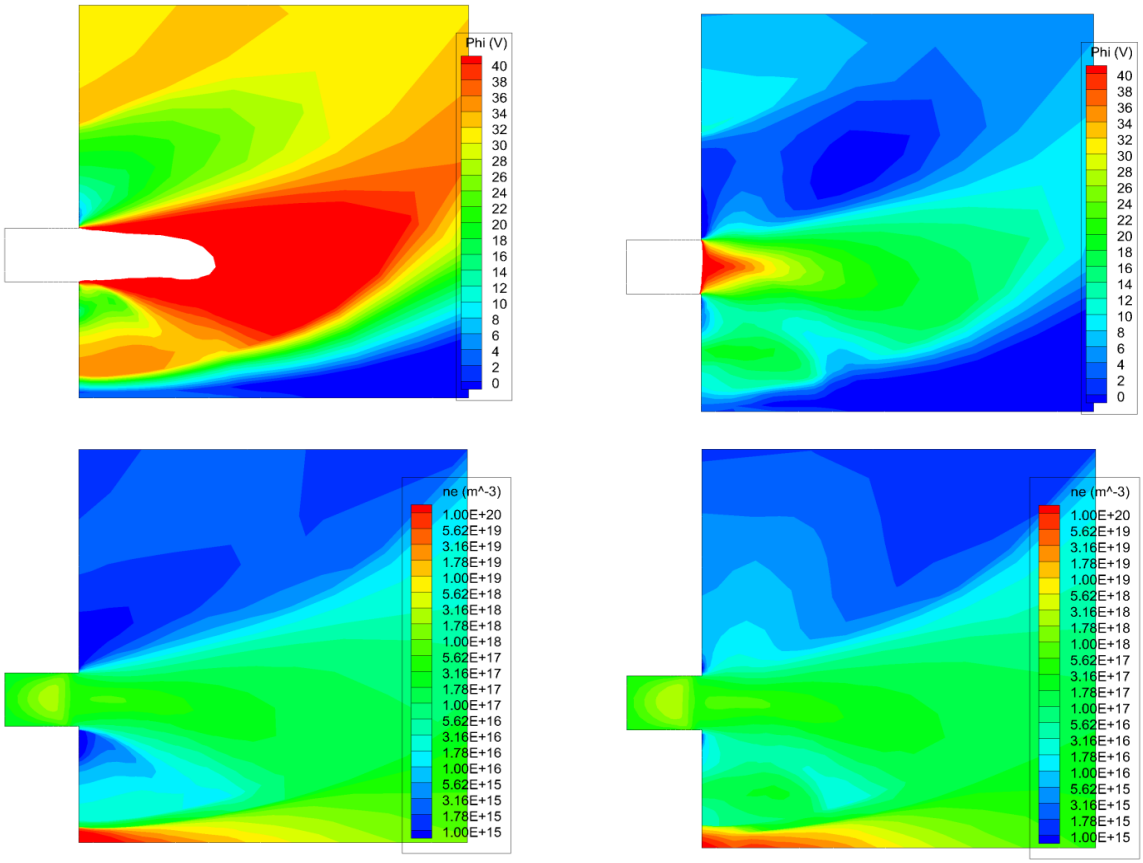

Fig. 6: Contour plots in the vacuum case. Top: Plasma potential (with color cut-off above 50V) Bottom: plasma density. Left column: Plasma properties when density accumulates close to the thruster axis. Notice the plasma potential wall that precludes the plasma to move radially after exiting the cathode and the low density in the inner pole region. Right column: Plasma properties after release. Density close to the axis has grown to very high values at ions start to overcome the potential wall. Resistivity decreases across cut-off B-line and the plasma potential decreases. Some electron current is allowed to cross to the inner pole region and discharge current increases.

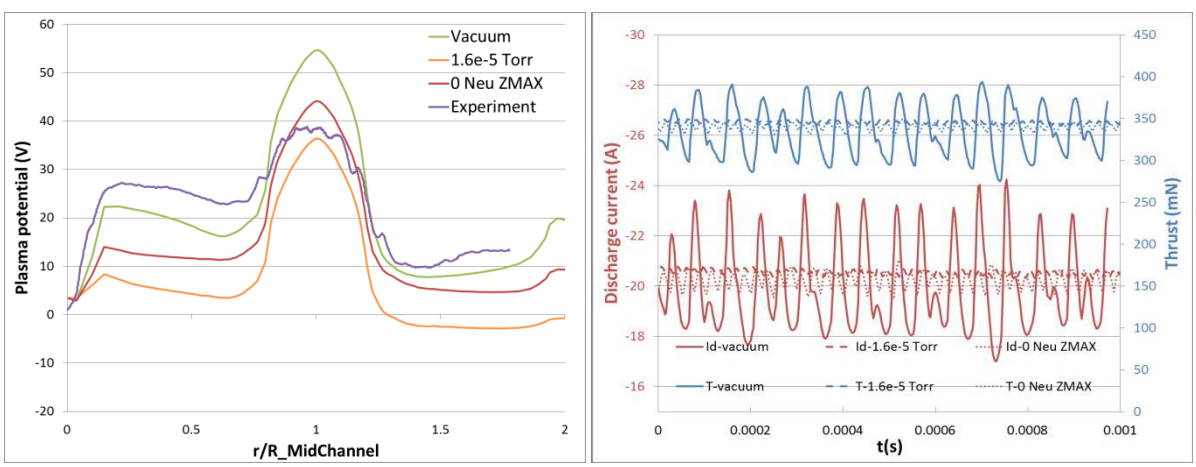

Fig. 7: Left: Comparison of radial profiles for plasma potential at z/L=1.19. The profile when the neutral gas density is set to zero at the right (ZMAX) boundary falls in between the vacuum and the isotropic background pressure cases. Right: Slightly larger oscillations in discharge current and thrust are predicted when neutral gas is removed from the ZMAX boundary.

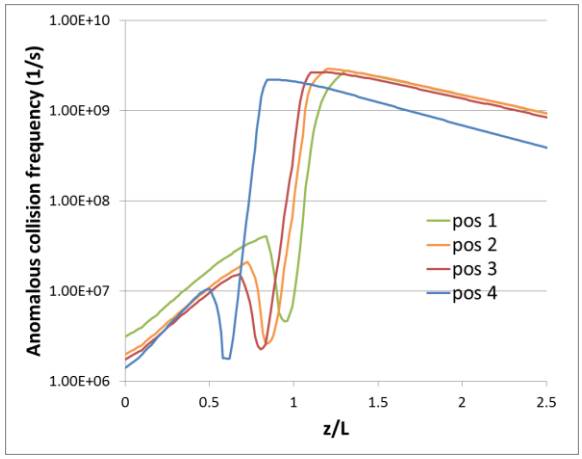

Fig. 8: Anomalous collision profiles at four different axial locations (positions 1 to 4). All cases produce the nominal discharge current of 20A.

B. Sensitivity of the computed plasma properties to the axial location of the anomalous collision frequency

The anomalous collision frequency profile depicted in Fig. 3 (left) is the result of careful examination of the effect that the anomalous collision frequency in each of the regions of the Hall thruster has in plasma parameters and performance [15,33,34]. For simplicity, we assume in this subsection a fixed shape of the profile and test the effect of shifting it from a downstream ("position 1") to an upstream position ("position 4"). The profile is also modified by multiplying it by a variable factor in order to obtain the nominal discharge current of 20 A without modifying the anode mass flow rate of neutral atoms into the thruster (Fig. 8). The four cases shown in this study were run with two fluids and background pressure of $1.6\text{x}10^{-5}$ Torr. Similarly to the case with background pressure shown in the previous subsection, these cases will not match the radial profile of the plasma potential at z/L =1.19. For this reason, we also include a case run in vacuum conditions for the anomalous collision frequency profile that matches more closely the experimental measurements in the radial direction.

Fig. 9 shows the plasma potential and electron temperature at the channel centerline produced by the four anomalous collision profiles presented in Fig. 8. Simulation results are compared to experimental measurements extracted from centerline and wall probes. Recent experimental investigations have clearly shown that centerline probes disturb the plasma inside the acceleration channel (roughly upstream from the point at which the magnitude of the applied of magnetic field peaks) so results from these probe measurements are only depicted downstream of

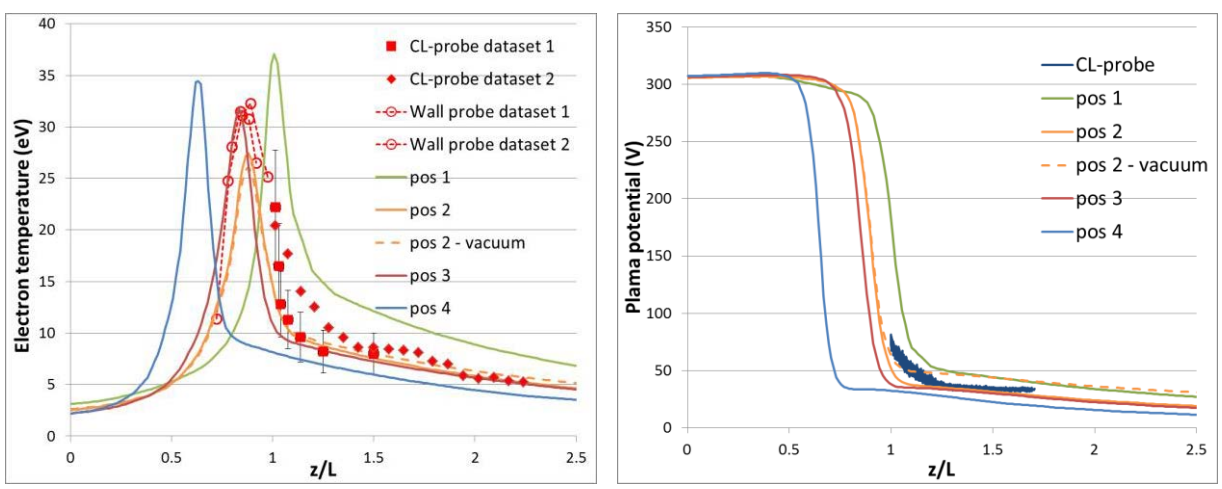

Fig. 9: Comparison of simulation results and measurements along the channel centerline of the H6 thruster for 4 different positions of the anomalous collision frequency profile. Left: electron temperature. Right: plasma potential. The experimental measurements are extracted from centerline and wall probes.

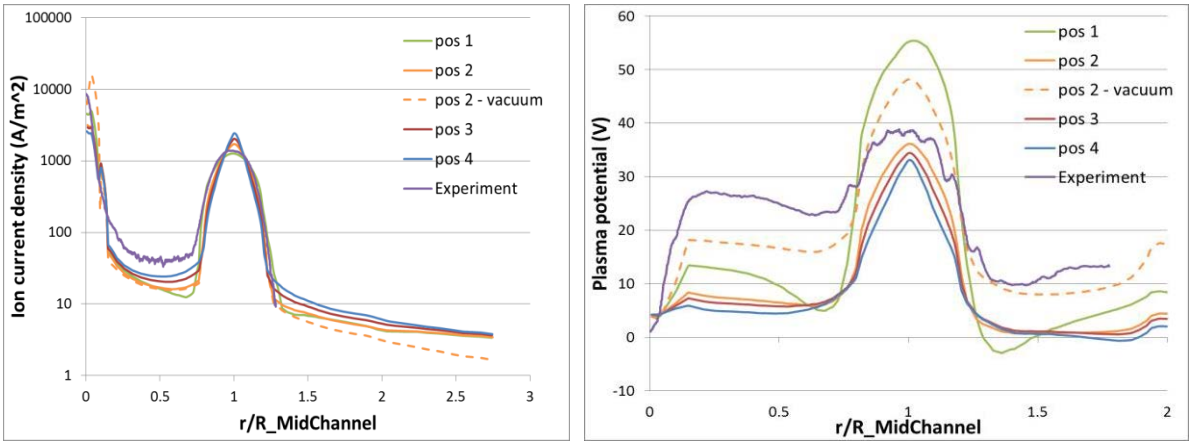

Fig. 10: Plasma parameters at z/L=1.19 for 4 different positions of the anomalous collision frequency profile. Left: ion current density. Right: Plasma potential. Ion current density does not change significantly between different cases since it is mainly driven by mass conservation. Plasma potential for position 2, 3 and 4 is very similar as z/L=1.19 is located far downstream from acceleration region. For position 1, z/L=1.19 is the downstream end of the acceleration region.

z/L=1. Wall probe data [35] has been extrapolated to the channel centerline assuming isothermality along magnetic field lines [36]. The best agreement with respect to experimental values is obtained when the profiles in position 2 and 3 are used. Profiles 1 and 4 are far downstream and upstream, respectively, of the desired location. Profile 3 matches the predicted peak in electron temperature more closely than profile 2 but it also decays from the peak temperature slightly upstream. With respect to the plasma potential, the second profile offers the best agreement. No major differences are found inside the acceleration channel in the vacuum case, which indicates that, as expected, background pressure effects are only relevant in the near plume region. As was shown in the previous subsection, the latter case predicts a higher value of the plasma potential downstream of the acceleration region.

As depicted in Fig. 10, the radial profiles of the plasma potential at *z/L*=1.19 are very similar for positions 2, 3 and 4. This is due to the acceleration region being positioned far upstream from this location. In the case of position 1, z/L=1.19 corresponds to the end of the acceleration region and, in consequence, the predicted potential is much higher. We also observe that the jump in plasma potential close to the cathode is steeper when the position 1 profile is used but this is likely to be driven by the higher value of the potential at the centerline. Ion current density is very similar in the four cases as it is dictated by mass conservation.

Table I summarizes performance parameters obtained with the four anomalous collision frequency profiles. Thrust is under-predicted in all cases by roughly 14% with position 2 giving the highest value at approximately 346mN. Since the differences in thrust between simulations are minor, changes in the position of the anomalous collision profile do not affect thrust significantly. Causes for the low values of thrust in simulations must lie in other models employed in the code and are currently under investigation.

Table I: Performance values for 4 different positions of the anomalous collision frequency profile.

	Position 1	Position 2	Position 2-vac	Position 3	Position 4	Measurements
Discharge current (A)	20	20	19.7	20	20	20
Thrust (mN)	344.0	346.2	336.6	341.3	335.6	401
Xe+ fraction	0.835	0.843	0.847	0.829	0.815	0.755
Xe++ fraction	0.156	0.150	0.146	0.161	0.173	0.161
Xe+++ fraction	0.009	0.008	0.007	0.010	0.012	0.084
Ion beam current (A)	14.21	14.09	14.40	13.64	13.73	16.71
Current utilization	0.71	0.70	0.72	0.68	0.69	0.835
Mass utilization	0.91	0.90	0.92	0.87	0.87	0.93
Anode efficiency	0.50	0.51	0.51	0.49	0.48	0.68

Considering all the results shown in this subsection, the position 2 profile offers the best overall agreement with experiments. The maximum value of electron temperature is better predicted by profile 3 but this profile is also located slightly upstream of the desired position. Profile 1 captures the jump in potential close to the cathode (Fig.10) but pushes the electron temperature and plasma potential profiles along the centerline far downstream of the desired location. Profile 2 also predicts the highest value for thrust, even though it is 14% lower than measured. Additional numerical experiments regarding the sensitivity of the computed plasma properties on the anomalous collision frequency may improve further our comparisons with the experiments. However, because the ultimate objective of identifying a profile that is as close to the unique solution as possible is to help guide investigations on the physics that can produce such profile, it is now evident here that any additional improvements in the comparisons would not alter significantly the anomalous collision frequency profile identified in this work.

C. Sensitivity of the computed plasma properties on multiple ion populations

We compare in this subsection plasma properties and performance parameters obtained with simulations that use 1, 2, or 3 fluids to model the motion of ions. The anomalous collision frequency profile that produced better agreement with the measurements (position 2) is used in all cases.

In Fig. 11, plasma potential and electron temperature are plotted along the channel centerline. They are compared to the experimental measurements that were also employed in the previous subsection. No major differences in plasma properties are encountered inside the acceleration channel due to the first fluid being dominant in that region. In the near plume region, the 1-fluid simulation predicts higher values of plasma potential and electron temperature due to the lower plasma density outside the acceleration channel.

Results shown in Fig. 12 for a radial profile close to the channel exit confirm that the simulations with 2 and 3 fluids predict almost identical results. For the 1-fluid case, the plasma density abruptly decreases near the poles. This results in gross underestimations of the ion current and plasma potential in these regions. In locations where the main beam and cathode beam are dominant, results of the three simulations are very similar, with the plasma potential being slightly higher at the channel centerline. Fig. 13 shows that thrust and discharge current are slightly lower when 1-fluid simulations are employed.

It is evident from the results shown in this subsection that the 1-fluid formulation is not suitable for predicting the plasma properties in the near plume. This is because when all ions are modeled by a single species, the velocity of high-energy ions becomes dominant and the whole pool of ions is assumed to move at higher speeds in the continuum approach. Due to mass conservation, this translates into lower plasma densities in regions away from the main and cathode beams of ions. However, single fluid simulations involve less computational costs and accurately predict conditions inside the acceleration channel. Performance variables are slightly affected by using a 1-fluid formulation but differences are in the order of 2 to 3%. Improvements by going to a 3-fluid model are negligible.

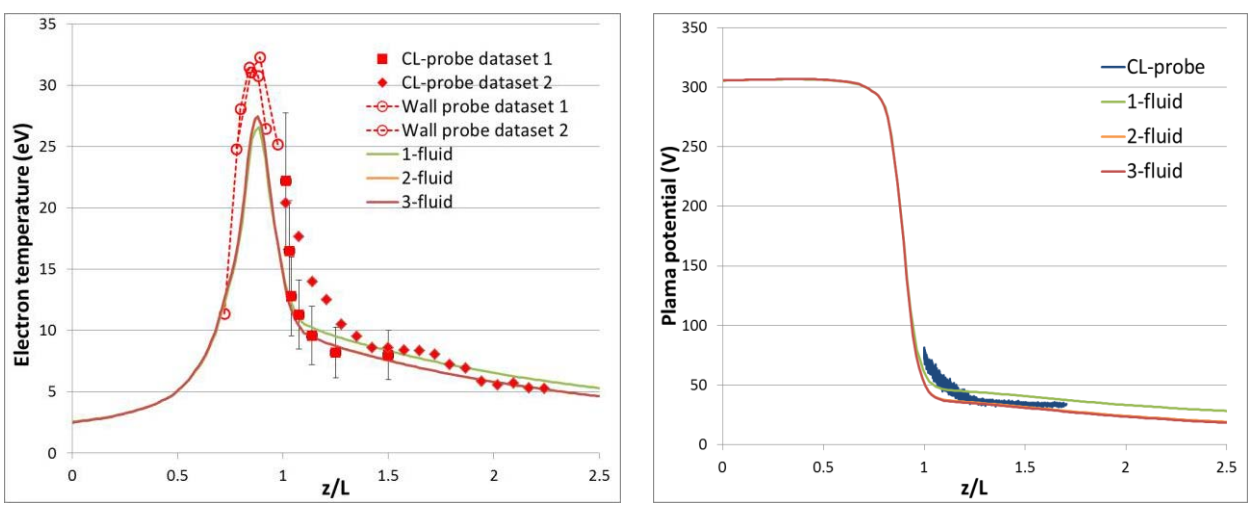

Fig. 11: Plasma properties at the centerline for simulations with 1, 2, and 3 fluids and anomalous collision frequency profile "position 2". Left: electron temperature. Right: plasma potential. No major differences are found between the 2- and 3-fluid cases, and for all cases inside the acceleration channel. When only 1 fluid is employed, electron temperature and plasma potential in the near plume increase due to lower plasma density.

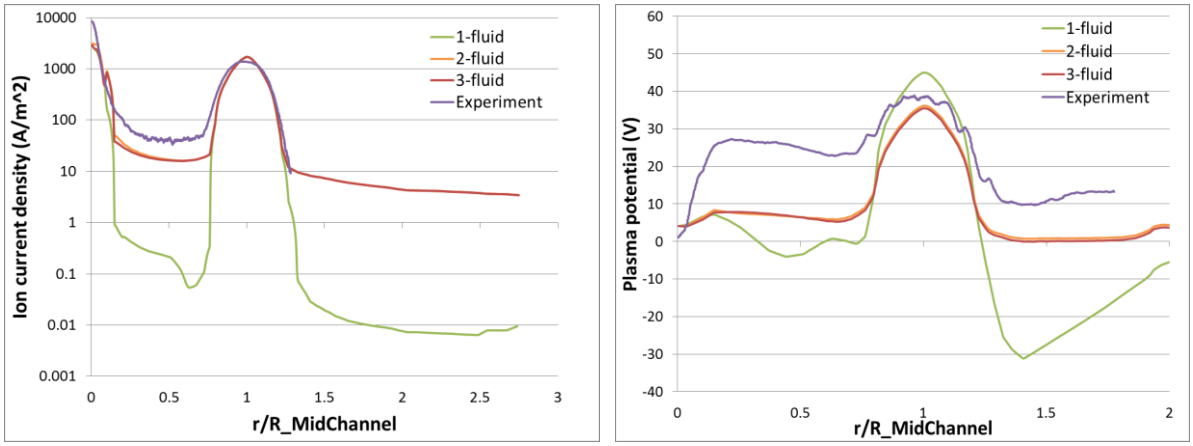

Fig. 12: Plasma properties at a radial profile located at z/L=1.19 for simulations with 1, 2, and 3 fluids and anomalous collision frequency profile "position 2". Left: total ion current density. Right: plasma potential. Simulation results with 2 and 3 fluids are almost identical. Major differences are encountered with respect to the 1-fluid case. Plasma density is very low in the inner and outer pole regions, which leads to low ion current density and negative values of the potential.

Thus, the 2-fluid model shall be used if the purpose of the simulation requires an accurate picture of the near plume (i.e., erosion of inner and outer poles) and the 1-fluid model can be used when simulations are intended to quantify performance variables or conditions inside the acceleration channel.

D. Channel erosion

We have determined so far an anomalous collision frequency profile that produces the closest agreement with experimental measurements. It was also shown that plasma properties inside the acceleration channel were not substantially modified by changes in the background pressure. The multi-fluid tests revealed that significant improvements in the solution of the near plume are achieved when a two-fluid simulation is employed. Splitting the flow of ions into more than two fluids does not substantially modify the plasma properties in our simulations. In this section, we examine whether the plasma properties obtained with the selected anomalous collision frequency profile are capable of reproducing the erosion rates found in experiments along the channel walls.

Erosion measurements have the advantage of not being disturbed by the probing method and offering a clear picture of the location of the plasma close to the thruster walls. On the other hand, several uncertainties exist in the erosion models. The expression used for computing the erosion rate at a boundary edge *b* is

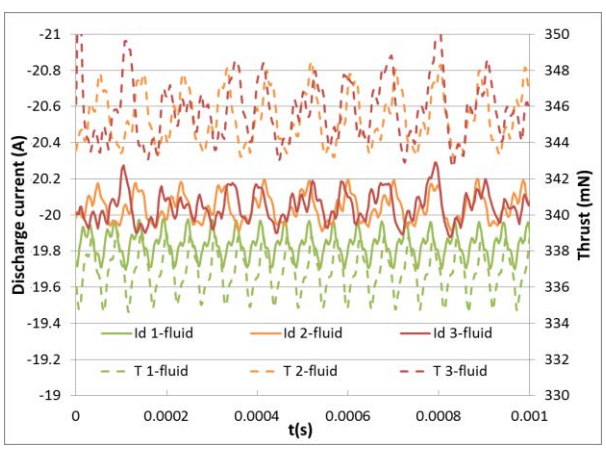

Fig. 13: Discharge current and thrust for simulations with 1, 2, and 3 fluids and anomalous collision frequency profile "position 2". Continuous lines: discharge current, dashed lines: thrust. Almost identical results are obtained for 2- and 3-fluid simulations. 1-fluid simulation predicts a 2.5 % lower value of thrust and 1.5% lower discharge current.

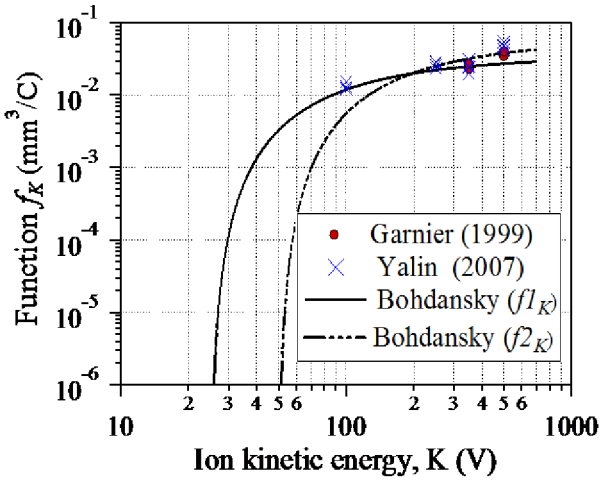

Fig. 14: Energy yield f_k as a function of ion energy in eV. Experimental measurements denoted by crosses and circles [37,38]. Two fits to the data using Bohdansky formula (33) are shown. These two curves represent the boundary of our uncertainty with respect to the threshold energy K_T.

$$\dot{\varepsilon}_b = \sum_{iF=1,nF} \sum_{iC=1,nC} q_{iC} n_{ic,iF,b} \mathbf{u}_b \cdot \hat{\mathbf{n}}_b Y_{sput,iC,iF,b} \,. \tag{31}$$

For each of the ion species, the contribution to the erosion rate is given by the current perpendicular to the wall multiplied by the sputtering yield, Y_{sput}. The sputtering yield is modeled as the product of two factors

$$Y_{sput,iC,iF,b} = f_{K,iC,iF,b} \left(\frac{Y(\theta)}{Y(0)} \right)_{iC,iF,b} \,. \tag{32}$$

The first term represents the sputtering yield as a function of the energy of ions at zero incidence angle while the second term accounts for the angle of incidence of ions. Fig. 14 depicts experimental measurements of f_k as a function of the ion energy K in eV from [37, 39]. These results are used to fit two curves that follow the expression proposed by Bohdansky [39]:

$$f_K = \begin{cases} C\left(1-\dfrac{K}{K_T}\right)^2 \left[1-\left(\dfrac{K}{K_T}\right)^{2/3}\right], \text{if } K \geq K_T \\ 0, \text{if } K < K_T \end{cases} . \tag{33}$$

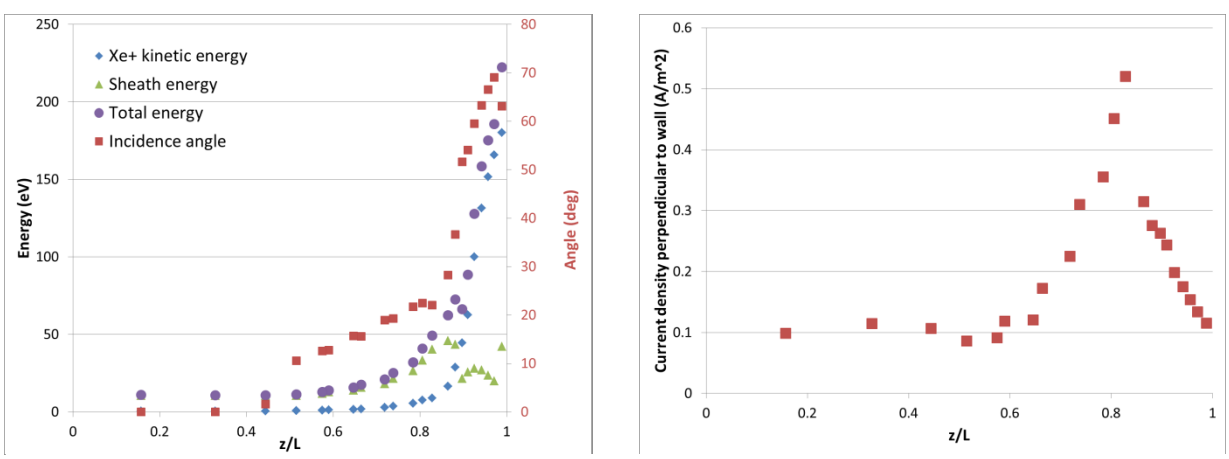

Fig. 15: Left: Energy and incidence angle of high energy, singly charged ions as a function of location in the inner channel wall. Total energy is the sum of pre-sheath kinetic energy and energy gained by acceleration in the sheath. Right: Current of high energy, singly charged ions perpendicular to the inner channel wall.

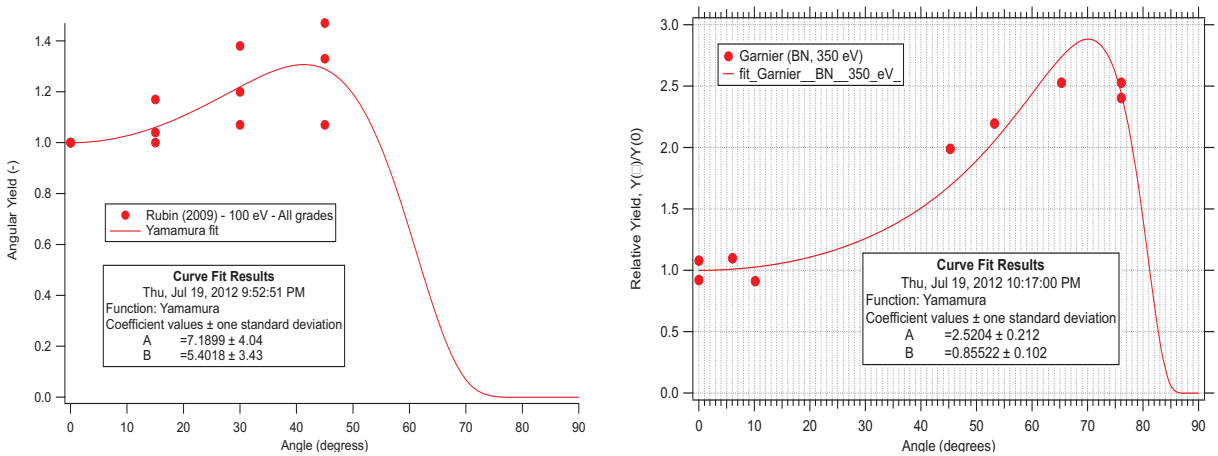

Fig. 16: Left: Rubin results for angular yield using 100eV ions and incidence angles up to 45 degrees. Right: Garnier data obtained using 350eV ions and incidence angles up to 80 degrees. Curves in both figures represent fit using Yamamura function (34) with coefficients A and B.

For the continuous line and dashed curves, respectively, C=0.035mm^3/C and K_T= 25eV, and C=0.06mm^3/C and K_T= 50eV. These two curves represent the boundaries of our uncertainty with respect to the threshold energy K_T. Fig. 15 shows the kinetic energy, sheath, and total energy of singly-charged ions of the high energy fluid (i.e., this species represents approximately 80% of the total ions impacting the walls) as a function of location at the inner wall. Similar results are obtained for the outer wall. The energy of ions increases from 25eV at z/L=0.6 to 50eV at z/L=0.8. Thus, the choice of threshold energy can have an important impact in determining the location where erosion begins. A second source of uncertainty is caused by the relative angular yield. As observed in Fig. 15 (left), the incidence angles range from 30 to 70 degrees in the locations where the ion energy is higher. Fig. 16 depicts two sets of data used for computing the relative angular yield. Experimental measurements are fitted using Yamamura's function [40]

$$\frac{Y(\theta)}{Y(0)} = \exp\left(-A\left[\frac{1}{\cos(\theta)}\right]\right)\cos(\theta)^B . \tag{34}$$

The first set of experimental results by Rubin [41] was measured using 100eV ions and only considers incidence angles up to 40 degrees. As a consequence, the relative yield decreases abruptly for angles greater than 60 degrees, resulting in high uncertainty for angular yields at high angles. The second set of data [37] considers 350eV with the relative yield measured up to angles of 80 degrees. The abrupt descent in the value of the function occurs for much higher angles. The angles used for these measurements are closer to our range of interest (i.e., 30 to 70 degrees according to Fig. 15 (left)) and therefore we can expect the Yamamura fit to be accurate for these high angles. However, the ion energy used is approximately 100eV higher than the typical values measured in the channel walls.

Fig. 17 shows the erosion rate computed per Eq. (31) using K_T=25,35, and 45 eV and Yamamura's fit to Rubin's and Garnier's data. Results using Rubin's data (left column) constantly under-predict the rate of erosion due to the function depicted in Fig. 16 (left) being almost zero there where the ion energy is high. Using the fit to Garnier's data produces results that are closer to the measurements due to the enhancing effect of the relative yield at high angles shown in Fig. 16 (right). Increasing the threshold energy K_T moves the location at which erosion begins downstream and also reduces the erosion rate for a given value of ion energy. Results using K_T=35eV and Yamamura's fit to Garnier's data offer the best agreement with experimental measurements. This study indicates that the plasma properties induced by the selected anomalous collision frequency profile is capable of acceptably reproducing erosion measurements within the range of uncertainty of the models used to predict the erosion rate. The only major difference between measurements and simulations occur at the channel exit, where the erosion rate decays in the simulation and remains monotonically increasing in experiments. This change of trend in Hall2De results is due to the current perpendicular to the wall decreasing in the acceleration zone, as seen in Fig. 15 (right). In the acceleration zone, the plasma density and electron temperature decrease. Plasma density changes are driven by mass continuity as the ions accelerate. Electron temperature controls the velocity of the ions into the wall through the sheath boundary condition (27). Results in the previous subsection showed that the drop in electron temperature downstream of the peak predicted by the simulation is slightly steeper than in the experimental measurements. A

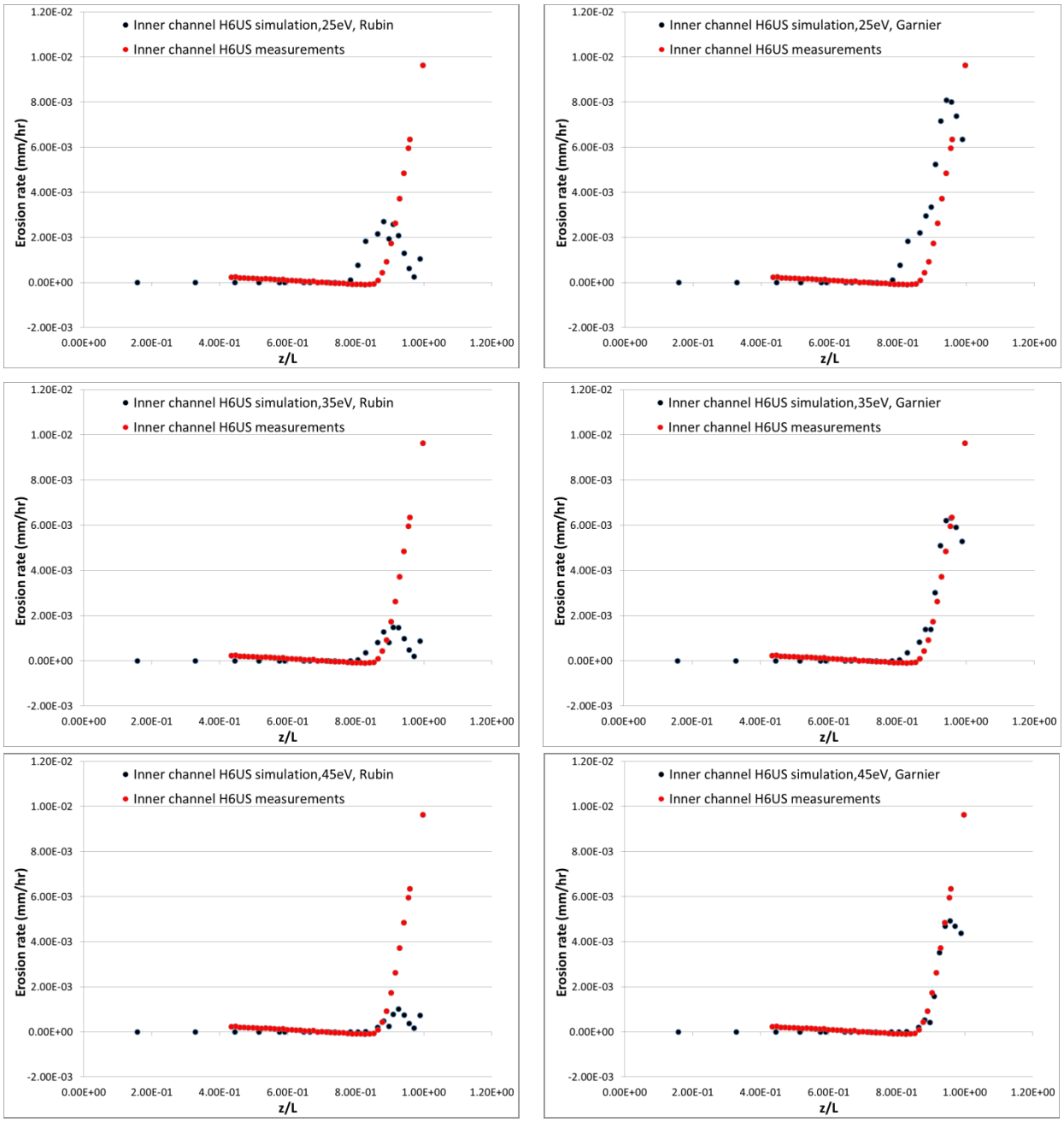

Fig. 17: Erosion rates at inner channel. Left column: Angular yield using Yamamura's function (34) fit to Rubin's data. Right column: Angular yield using Yamamura's function (34) fit to Garnier's data. Rows: Threshold energy K_T in Eq.(33) set to 25, 35, and 45 eV., respectively.

more gentle decrease in the electron temperature would increase the perpendicular ion current close to the channel exit and the erosion rate.

III. Conclusion

We have advanced the capabilities of the Hall2De code by implementing a new algorithm for the ion hydrodynamics. The new algorithm employs a conservative, finite volume, cell-centered method that can be applied to different types of grids (not only the magnetic-field-aligned grid used in Hall2De). Savings in computational time by factors as high as 4 are achieved by evolving the equations of motion implicitly in time using a predictor/multi-corrector algorithm.

Hydrodynamics formalisms convect mass elements using averaged velocities, which can potentially result in unphysical results when high- and low-speed particles that do not have time to equilibrate are present at a given location. This difficulty is addressed by the implementation of a multi-fluid algorithm that treats separately ions of different energy. Different species still interact between one another through elastic and inelastic collisions. Simulations that make use of the multi-fluid approach exhibit higher values of the plasma density and potential in the near plume region, bringing results closer to experimental measurements. This improvement is of significance to pole erosion assessments.

We showed multiple comparisons with experimental measurements with the aim of validating the large changes introduced in Hall2De. The hypothesis that classical collisions are dominant close to the cathode was shown to be accurate as the drop in plasma potential in this region observed in probe measurements cannot be reproduced if the anomalous mechanisms were dominant over classical collisions. The resistivity, which controls the extent of the potential jump across magnetic fields lines, increases when only classical collisions are considered and depends approximately on the inverse square of the plasma density. This leads simulations in vacuum to predict results that are closer to the experimental measurements that those obtained in the presence of background pressure. In the latter case, the potential wall is under-predicted due to the increased plasma density (i.e., lower resistivity) resulting from enhanced ionization due to facility effects. Oscillations with frequencies close to those reported for breathing-mode oscillations are observed in the vacuum case. We also identified an anomalous collision frequency profile that produces plasma parameters in agreement with probe measurements at the channel centerline, which will allow us to pursue the possible physics that can produce it. This profile is not significantly different than that identified in earlier simulations with Hall2De. Thrust predictions are not significantly affected by changes in the location of the anomalous collision frequency profile and they consistently under-predict measurements by approximately 13%. Finally, we showed results of erosion rate models based on plasma properties at the channel walls obtained from numerical simulations. Computed erosion profiles appear to be highly dependent on the incidence angle between the ions and the walls, especially when angles are over 60 degrees. The threshold energy below which there is no sputtering (estimated to be between 25 and 50 eV) has an impact on the location along the channel at which erosion begins. Comparison with experimentally measured rates of erosion reveals that we are able to accurately match the predicted erosion within the cited uncertainties.

Future work will focus on understanding the source of the low thrust values predicted in these most recent simulations. Results are shown to under-predict the flow of triply charged ions by a factor of 8, which may account for about half of the difference in thrust between experiments and simulations. The relevant collision cross sections will therefore be revisited. We also plan to investigate how to model the background pressure at the boundaries of the computational domain to account for deviations in isotropy. It has been shown that these deviations have a profound influence on the plasma properties in the near plume (i.e., the drop in potential close to the cathode).. Finally, we need to apply the knowledge gained from the investigations performed on the effect of the anomalous collision frequency on the plasma properties in the understanding of the physical mechanisms that reduce resistivity across magnetic field lines in Hall-effect thrusters.

Acknowledgments

The research described in this paper was carried out by the Jet Propulsion Laboratory, California Institute of Technology, under a contract with the National Aeronautics and Space Administration. The authors wish to acknowledge Dr. Ira Katz for the useful comments and discussions on the content of this manuscript.

References

[1] A. I. Morozov, Vestnik Akademii Nauk SSSR, Vol 15, 1974 (in Russian).

[2] A. I. Morozov and I. V. Melikov, Journal of Technical Physics, Vol 44, 1974, p.544 (in Russian).

[3] B. I. Volkov, A. I. Morozov, A. G. Sveshnikov, and S. A. Iakunin, Fiz. Plazmy Vol.7, 1981, p.245 (in Russian).

[4] C. K. Birdsall and A. B. Langdon, "Plasma Physics via Computer Simulation", Adam Hilger, ed., Bristol, England, UK, 1991.

[5] M. Hirakawa and Y. Arakawa, "Numerical simulation of plasma particle behavior in a Hall thruster", AIAA paper 96-3195, in proceedings of the 32nd AIAA Joint Propulsion Conference, Lake Buena Vista, Florida, 1996, p. 3195

[6] J. M. Fife, Ph.D. thesis, Massachusetts Institute of Technology, 1998.
[7] I. Parra, E. Ahedo, J. M. Fife, and M. Martinez-Sanchez, "A two-dimensional hybrid model of the Hall thruster discharge", Journal of Applied Physics, Vol. 100, 2006, p. 023304.
[8] J. M. Fife, M. Martinez-Sanchez, and J. Szabo, "A numerical study of low-frequency discharge oscillations in Hall thrusters", AIAA paper 1997-3052, in proceedings of the 33rd AIAA Joint Propulsion Conference, Seattle, WA, 1997.
[9] J. P. Boeuf and L. Garrigues, "Low Frequency Oscillations in a Stationary Plasma Thruster," Journal of Applied Physics, Vol. 84, 1998, p. 3541.
[10] S. Barral and E. Ahedo, "Low-frequency model of breathing oscillations in Hall discharges", Physical Review E, Vol. 79, 2009, p. 046401.
[11] M. Keidar, I. D. Boyd, and I. I. Beilis, "Plasma flow and plasma-wall transition in Hall thruster channel", Physics of Plasmas, Vol. 8, 2001, p. 5315.
[12] I. G. Mikellides and I. Katz, "Numerical simulations of Hall-effect plasma accelerators on a magnetic-field-aligned mesh", Physical Review E, Vol. 86, 2012, p. 046703.
[13] R. Marchand and M. Dumberry, "CARRE: a quasi-orthogonal mesh generator for 2D edge plasma modelling", Computer Physics Communications, Vol. 96, 1996, pp. 232-246.
[14] Z. Lin, T. S. Hahm, W. W. Lee, W. M. Tang, and R. B. White, "Turbulent Transport Reduction by Zonal Flows: Massively Parallel Simulations," Science, Vol. 281, 1998, pp. 1835-1837.
[15] I. G. Mikellides, I. Katz, and R. R. Hofer, "Design of a laboratory Hall thruster with magnetically shielded channel walls, phase I: numerical simulations", AIAA paper 2011-5809, in proceedings of the 47th AIAA Joint Propulsion Conference, San Diego, California, 2011.
[16] D. J. Bohm, E. Burhop, and H. Massey, "Characteristics of electrical discharges in magnetic fields", in National Nuclear Energy Series, Manhattan Project Technical Section, Division I, Guthrie, A. and Waterling, R. K., Eds., McGraw-Hill, New York, 1949.
[17] I. G. Mikellides, A. Lopez Ortega, and B. Jorns, "The sensitivity of the acceleration zone on the anomalous collision frequency and implications on erosion predictions in simulations of magnetically shielded Hall thrusters", AIAA paper 2014-xxxx, in proceedings of the 50th AIAA Joint Propulsion Conference, Cleveland, Ohio, 2014.
[18] B. M. Reid, "The Influence of Neutral Flow Rate in the Operation of Hall Thrusters," Ph.D. Thesis, Aerospace Engineering, University of Michigan, 2009.
[19] D. L. Brown, C. W. Larson, J. M. Haas, and A. D. Gallimore, "Analytical extraction of plasma properties using a Hall thruster efficiency architecture", IEPC paper 2007-188, in proceedings of the 30th International Electric Propulsion Conference, Florence, Italy, 2007.
[20] I. G. Mikellides, I. Katz, R. R. Hofer, and D. M. Goebel, "Hall-effect thruster simulations with 2-D electron transport and hydrodynamic ions", IEPC paper 2009-114, in proceedings of the 31st International Electric Propulsion Conference, Ann Arbor, Michigan, 2009.
[21] C. Hirt and B. Nichols, "Volume of fluid (VOF) method for the dynamics of free boundaries", Journal of Computational Physics, Vol. 39, 1981, pp. 201-225
[22] P. T. Barton, R. Deiterding, D. I. Meiron, and D. I. Pullin, "Eulerian adaptive finite-difference method for high-velocity impact and penetration problems", Journal of Computational Physics, Vol. 240, 2013, pp. 76-99
[23] S. P. van der Pijl, A. Segal, C. Vuik, and P. Wesseleng, "A mass-conserving level-set method for modelling of multi-phase fluids", International Journal for Numerical Methods in Fluids, Vol. 47, 2005, pp. 339-361
[24] R. Rejoub, B. G. Lindsay, and R. F. Stebbings, "Determination of the absolute partial and total cross sections for electron-impact ionization of the rare gases", Physical Review A, Vol. 65, 2002, pp. 042713.
[25] W. Bell, N. Djuric, and G. H. Dunn, "Electron –impact ionization of In^+ and Xe^+", Physical Review A, Vol. 48, 1993, pp. 4286.
[26] I. Borovik, J. Rausch, J. Rudolph, M. Gharaibeh, S. Schippers and A. Muller, "Electron impact ionization of Xenon ions", Journal of Physics: Conference Series, Vol. 194, Part 6, 2009, pp, 062014.
[27] J. S. Miller, S. H., Pullins, D. J. Levandier, Y. H. Chiu, and R. A. Dressler, "Xenon charge exchange cross sections for electrostatic thruster models", Journal of Applied Physics, Vol. 91, No. 3, 2002, pp. 984-991.
[28] I. Katz and I. G. Mikellides, "Neutral gas free molecular flow algorithm including ionization and walls for use in plasma simulations", Journal of Computational Physics, Vol. 230, 2011, pp. 1454-1464
[29] A. Harten, P. Lax, and B. Leer, "On upstream differencing and Godunov-type schemes for hyperbolic conservation laws", SIAM review 25, 1983, pp. 35-61.
[30] R. Courant, K. Friedrichs, and H. Lewy, "On the partial difference equations of mathematical physics", IBM Journal of Research and Development, Vol. 11, 1928, pp. 215-234.
[31] J. C. Butcher, "Numerical methods for ordinary differential equations", John Wiley & sons, New York, 2003.

[32] K. U. Riemann, "The Bohm criterion and sheath formation", Journal of Physics D: Applied Physics, Vol. 24, 1991, p. 493.

[33] R. R. Hofer, D. M. Goebel, I. G. Mikellides, and I. Katz, "Design of a laboratory Hall thruster with magnetically shielded channel walls, phase II: experiments", AIAA paper 2012-3788, in proceedings of the 48th AIAA Joint Propulsion Conference, Atlanta, Georgia, 2012.

[34] I. G. Mikellides, R. R. Hofer, I. Katz, and D. M. Goebel, "The effectiveness of magnetic shielding in high I_{sp} Hall thrusters", AIAA paper 2013-3885, in proceedings of the 49th AIAA Joint Propulsion Conference, San Jose, California, 2013.

[35] R. R. Hofer, D. M. Goebel, I. G. Mikellides, and I. Katz, "Magnetic shielding of a laboratory Hall thruster Part II: experiments," Journal of Applied Physics, Vol. 115, 2014, p. 043304.

[36] I. G. Mikellides, I. Katz, R. R. Hofer, and D. M. Goebel, "Magnetic shielding of a laboratory Hall thruster, Part I: theory and validation," Journal of Applied Physics, Vol. 115, 2014, p. 043303.

[37] Y. Garnier, V. Viel, J. F. Roussel, and J. Bernard, "Low-energy xenon ion sputtering of ceramics investigated for stationary plasma thrusters", Journal of Vacuum Science and Technology A, Vol. 17, 1999, pp. 3246-3254

[38] A. P. Yalin, B. Rubin, S. R. Dominguez, Z. Glueckert, and J. D. Williams, "Differential sputter yields of boron nitride, quartz and kapton due to low energy Xe+ bombardment", AIAA paper 2007-5314, in proceedings of the 43rd AIAA Joint Propulsion Conference, Cincinnatti, Ohio, 2007.

[39] J. Bohdansky, J. Roth, and H. L. Bay, "An analytical formula and important parameters for low-energy ion sputtering", Journal of Applied Physics, Vol. 51, 1980, p. 1610.

[40] Y. Yamamura and S. Shindo, "An empirical formula for angular dependence of sputtering yields", Radiation Effects, Vol. 80, 1984, pp. 52-72.

[41] Rubin, J. L. Topper, and A. P. Yalin, "Total and differential sputter yields of boron nitride measured by quartz crystal microbalance", Journal of Physics D: Applied Physics, Vol. 42, 2009, p.205205